

# Substitution Effect on the Photocatalytic Degradation by the Series $A_x\text{Bi}_{26-x}\text{Mo}_{10}\text{O}_{68+0.5y}$ ( $A = \text{Ba}, y = 0$ ; $A = \text{Bi}, \text{La}, y = 2$ ): A Kinetic Study

B. Muktha,<sup>†</sup> T. Aarthi,<sup>‡</sup> Giridhar Madras,<sup>‡</sup> and T. N. Guru Row<sup>\*,†</sup>

Solid State and Structural Chemistry Unit and Department of Chemical Engineering, Indian Institute of Science, Bangalore 560012, India

Received: February 14, 2006; In Final Form: April 4, 2006

The compounds  $\text{Ba}_2\text{Bi}_{24}\text{Mo}_{10}\text{O}_{68}$  and  $\text{La}_2\text{Bi}_{24}\text{Mo}_{10}\text{O}_{69}$  were synthesized by the ceramic route and characterized by single crystal and powder X-ray diffraction, respectively. The structure of these phases is isostructural with that of  $\text{Bi}_{26}\text{Mo}_{10}\text{O}_{69}$ . Along the  $b$  axis columns of  $[\text{Bi}_{12}\text{O}_{14}]$  units are separated by  $\text{MoO}_4$  tetrahedra and noncolumnar A ( $A = \text{Ba}, \text{La}$ ) atoms. UV–visible spectra of  $\text{Bi}_{26}\text{Mo}_{10}\text{O}_{69}$ ,  $\text{Ba}_2\text{Bi}_{24}\text{Mo}_{10}\text{O}_{68}$ , and  $\text{La}_2\text{Bi}_{24}\text{Mo}_{10}\text{O}_{69}$  suggest that band gap decreases on substitution of La and Ba for Bi at the noncolumnar site. The photocatalytic degradation of water pollutants such as phenol and substituted phenols was studied. All the catalysts show specificity toward nitro substituent at the para position in the aromatic ring.

## Introduction

Bismuth molybdates have been well studied in terms of structure owing to their properties such as conductivity,<sup>1,2</sup> ferroelectricity,<sup>3</sup> and catalysis.<sup>4,5</sup> Several of the bismuth molybdates have fluorite-related structure and are good oxide ion conductors.<sup>6,7</sup> The most complex phase among them,  $\text{Bi}_{26}\text{Mo}_{10}\text{O}_{69}$  represents a solid solution around  $x\text{Bi}_2\text{O}_3\text{--}\text{MoO}_3$  in the range,  $1.3 \leq x \leq 1.7$ .<sup>8</sup> The crystal structure was shown to consist of infinite columns of  $[\text{Bi}_{12}\text{O}_{14}]$  units surrounded by noncolumnar Bi atoms and isolated  $\text{MoO}_4$  tetrahedra.  $\text{Bi}_{26}\text{Mo}_{10}\text{O}_{69}$  shows a conductivity value of the order  $\sim 10^{-3} \text{ S cm}^{-1}$  at 600 °C. Substitution of Pb at the noncolumnar Bi atom site  $\text{Bi}_{26}\text{Mo}_{10}\text{O}_{69}$  resulted in an isostructural phase,  $\text{PbBi}_{12}\text{Mo}_5\text{O}_{34}$ .<sup>9</sup> Interestingly the coordination of the noncolumnar atom changes from eight in  $\text{Bi}_{26}\text{Mo}_{10}\text{O}_{69}$  and four in  $\text{PbBi}_{12}\text{Mo}_5\text{O}_{34}$ , respectively. Subsequently isostructural phases of the type,  $\text{Bi}(\text{Bi}_{12-x}\text{Te}_x\text{O}_{14})\text{--}\text{Mo}_{4-x}\text{V}_{1+x}\text{O}_{20}$  ( $0 \leq x \leq 2.5$ ),<sup>10</sup>  $\text{BiMo}_{10-x}\text{W}_x\text{O}_{69}$ ,<sup>11</sup>  $\text{BiMo}_{10-x}\text{V}_x\text{O}_{69}$ ,  $\text{BiMo}_{10-x}\text{P}_x\text{O}_{69}$ ,<sup>8</sup>  $\text{Bi}_{26-x}\text{A}_x\text{Mo}_{10}\text{O}_{69-0.5x}$  ( $A = \text{Pb}, \text{Ca}, \text{Sr}, \text{Ba}$ ), and  $\text{A}_2\text{Bi}_{24}\text{Mo}_8\text{X}_2\text{O}_{68}$  ( $X = \text{Cr}, \text{W}$ )<sup>12</sup> were isolated and found to have good electrical properties particularly in those containing tungsten.

Grins et al.<sup>13</sup> reported the crystal structure of  $\text{Bi}_6\text{Cr}_2\text{O}_{15}$  in the orthorhombic  $Ccc2$  space group with  $a = 12.30184$  (5),  $b = 19.87492$  (7), and  $c = 5.88162$  (2) Å solved based on neutron diffraction data. The structure is built of  $[\text{Bi}_{12}\text{O}_{14}]$  units surrounded by noncolumnar Bi atoms and isolated  $\text{CrO}_4$  tetrahedra. The value of conductivity was of the order of  $10^{-5} \text{ cm}^{-1}$  at 600 °C. The oxide ion conductivity in these materials was found to occur through the  $\text{MoO}_4$  tetrahedra.<sup>14</sup>

It is of interest to evaluate the photophysical properties of these materials and their effects on substitution. In our study, we have synthesized  $\text{Bi}_{26}\text{Mo}_{10}\text{O}_{69}$ ,  $\text{Ba}_2\text{Bi}_{24}\text{Mo}_{10}\text{O}_{68}$ , and  $\text{La}_2\text{Bi}_{24}\text{Mo}_{10}\text{O}_{69}$  and have investigated their photocatalytic properties. In this article we report the single-crystal X-ray structure of  $\text{Ba}_2\text{Bi}_{24}\text{Mo}_{10}\text{O}_{68}$  and the substitution effect of La

and Ba at the noncolumnar site in  $\text{Bi}_{26}\text{Mo}_{10}\text{O}_{69}$  in the photocatalytic degradation of water pollutants such as phenol, 4-chlorophenol, 4-nitrophenol, 4-methylphenol, 4-chloro-2-nitrophenol and 4-nitro-2-chlorophenol, 2,4-dinitrophenol, and 2-nitrophenol under UV radiation.

## Experimental Section

**Synthesis and Crystallization.**  $\text{Bi}_2\text{O}_3$  (Fluka, 99.99%) and  $\text{La}_2\text{O}_3$  (Sigma Aldrich, 99.99%) were dried at 600 °C for 4 h.  $\text{BaCO}_3$  (Fluka, 99%) and  $\text{MoO}_3$  (Fluka, 99%) were used as obtained. Polycrystalline phases of all the phases were synthesized by the ceramic method.<sup>8</sup> The progress of the reactions was monitored by powder X-ray diffraction that confirmed the formation of a single phase each for  $\text{Ba}_2\text{Bi}_{24}\text{Mo}_{10}\text{O}_{68}$  and  $\text{Bi}_{26}\text{Mo}_{10}\text{O}_{69}$  and two phases in the case of  $\text{La}_2\text{Bi}_{24}\text{Mo}_{10}\text{O}_{69}$ .

Single crystals of  $\text{Ba}_2\text{Bi}_{24}\text{Mo}_{10}\text{O}_{68}$  and  $\text{La}_2\text{Bi}_{24}\text{Mo}_{10}\text{O}_{69}$  were obtained by melting the polycrystalline samples at 1100 °C for 1 h in a platinum crucible followed by slow cooling at 1 °C/h to 950 °C and then slowly cooling to room temperature. In the case of  $\text{La}_2\text{Bi}_{24}\text{Mo}_{10}\text{O}_{69}$ , the presence of two phases was observed under an optical microscope. The single crystals formed the major phase while the minor phase was polycrystalline in nature. Single crystals were carefully physically separated from the mixture under the microscope. A part of these single crystals was ground well, and the powder pattern was recorded to confirm the purity of the phase (See Figure S1, Supporting Information). The separated single crystals were powdered and were used for the conductivity and photocatalytic experiments

**Characterization. Powder X-ray Diffraction.** Powder X-ray diffraction data were collected at room temperature on a Philips X' Pert Pro diffractometer, using  $\text{Cu K}\alpha$  radiation. Data were collected over the angular range  $5^\circ \leq 2\theta \leq 100^\circ$  in steps of  $\Delta(2\theta) = 0.02^\circ$ . The high-temperature powder data were collected on a platinum sample holder, and the powder patterns were collected for every 10 °C increase in temperature from 280 to 350 °C. The powder diffraction pattern obtained after the heating and cooling cycles did not show any change suggesting the reversibility of the phase transition.

\* To whom correspondence should be addressed. Tel: +91-80-22932796, +91-80-22932336. Fax: +91-80-23601310. E-mail: sscnrg@sscu.iisc.ernet.in.

<sup>†</sup> Solid State and Structural Chemistry Unit.

<sup>‡</sup> Department of Chemical Engineering.

**TABLE 1: Crystallographic Data for Ba<sub>2</sub>Bi<sub>24</sub>Mo<sub>10</sub>O<sub>68</sub>**

empirical formula	Ba <sub>2</sub> Bi <sub>24</sub> Mo <sub>10</sub> O <sub>68</sub>
crystal habit, color	cylindrical, yellow
crystal Size (mm)	0.248 × 0.131 × 0.086
crystal system	monoclinic
space group	<i>P</i> 2/ <i>c</i>
cell dimensions (Å/deg)	<i>a</i> = 11.688(4) <i>b</i> = 5.813(1) <i>c</i> = 24.715(7) $\beta$ = 101.838(4)
volume (Å <sup>3</sup> )	1643.8(8)
formula weight	3068
<i>D<sub>x</sub></i> (g/cm <sup>3</sup> )	7.4097
<i>Z</i>	8
<i>F</i> (000)	929
scan mode	phi-scan
$\theta$ max	27.92
recording reciprocal space	$-15 \leq h \leq 13, -7 \leq k \leq 7, -31 \leq l \leq 32$
no. of independent reflections	2942 [ <i>R</i> (int) = 0.0326]
$\mu$ (mm <sup>-1</sup> )	67.081
refinement	<i>F</i> <sup>2</sup>
no. of variables	76
<i>R</i> ( <i>F</i> )	0.0558
w <i>R</i> ( <i>F</i> <sup>2</sup> )	0.1374
GoF	1.24
max/min Dr e/Å <sup>3</sup>	6.225/−4.41

**EDX Analysis.** Metal compositions of Ba<sub>2</sub>Bi<sub>24</sub>Mo<sub>10</sub>O<sub>68</sub> and La<sub>2</sub>Bi<sub>24</sub>Mo<sub>10</sub>O<sub>69</sub> were determined from eight-point energy dispersive X-ray (EDX) analysis (JEOL JSM-840) on single-crystal surfaces. Four different points on the crystals were checked for the ratio of the metal ions. The ratio of the Bi/Mo/A ions thus calculated from the EDX analyses corresponded to that of the ions taken initially for syntheses.

**Single-Crystal X-ray Diffraction.** Single-crystal X-ray diffraction data were collected on a Bruker AXS SMART APEX CCD diffractometer<sup>15</sup> with a crystal to detector distance of 6.06 cm. The data were collected based on three sets of runs covering a complete sphere of reciprocal space with each set at different  $\varphi$  angle ( $\varphi = 0, 90, 180^\circ$ ). Each frame covered  $0.3^\circ$  in  $\omega$ . The data were reduced using SAINT PLUS,<sup>15</sup> and the structure was solved by direct methods using SHELXS97<sup>16</sup> and refined using JANA2000.<sup>17</sup> Crystallographic data and the details of the single-crystal data collection are given in Table 1.

The UV–visible diffuse reflectance spectra were recorded on a Perkin-Elmer Lambda 35 UV–visible spectrophotometer. DTA was performed on a SDTQ600 DSC/DTA instrument, under a constant flow nitrogen atmosphere. Thermogravimetric analysis of the samples indicates no weight loss on heating the sample over a temperature range from room temperature to 600 °C.

**ac Impedance.** A circular pellet of La<sub>2</sub>Bi<sub>24</sub>Mo<sub>10</sub>O<sub>69</sub> of about 10 mm thickness sintered at 600 °C was sputtered with gold for ac impedance measurements. The sample was then mounted in an impedance jig and placed in a tube furnace in which the temperature was controlled to  $\pm 3$  °C over the range 30–700 °C. ac impedance measurements were carried out between 5 Hz and 13 MHz on a Hewlett-Packard HP4192A impedance gain phase analyzer. A home-built cell assembly with a two-terminal capacitor configuration and stainless steel electrodes was used for the experiment. The sample temperature was measured using a Pt–Rh thermocouple positioned very close to the sample. The frequency dependence of the impedance was measured between 30 and 700 °C in a heating–cooling cycle. The ionic conductivity was calculated from the intercept of the single semicircular arcs obtained in the complex impedance plots.

**Photocatalytic Experiments. Photochemical Reactor.** The details of the photochemical reactor employed in this study have been reported elsewhere.<sup>18</sup> A high-pressure mercury vapor lamp (HPML) (125 W, Philips, India) was used for the degradation reactions. The lamp radiated predominantly at 365 nm corresponding to an energy of 3.4 eV.

**Degradation Experiments.** Powder samples of Ba<sub>2</sub>Bi<sub>24</sub>Mo<sub>10</sub>O<sub>68</sub> and Bi<sub>26</sub>Mo<sub>10</sub>O<sub>69</sub> were used for the degradation reactions. In the case of La<sub>2</sub>Bi<sub>24</sub>Mo<sub>10</sub>O<sub>69</sub>, a powdered sample of crushed single crystals (separated from the minor phase) was used. The phenolic compounds were dissolved in double distilled Millipore filtered water. The degradation reactions were performed in a photochemical reactor with various initial concentrations with a constant catalyst concentration of 1.0 kg/m<sup>3</sup>. Samples were collected at regular intervals for subsequent analysis. Control experiments conducted without the catalyst under UV radiation and with the catalyst without UV radiation did not show any appreciable degradation indicating that both the catalyst and UV radiation are required for the degradation reactions. There was only about 1% reduction in the concentration of all compounds of interest when a solution of 100 ppm was stirred with the catalysts (at a loading of 1 kg/m<sup>3</sup>) for 12 h in dark. Therefore, the actual concentration of the solution was taken to be the initial concentration for kinetic analysis. The optimal catalyst loading of the catalyst was found to be 1 kg/m<sup>3</sup> with no significant increase in the degradation of organics for higher concentrations of the catalysts. Hence, this catalyst concentration was used for all the photocatalytic degradation experiments. The reactions were carried out at natural pH conditions with the initial concentrations between 10 and 200 ppm for all phenols depending on their emissivity at  $\lambda_{\text{max}}$  in the UV spectra.

**Sample Analysis.** The degraded samples were filtered through Millipore membrane filters and centrifuged to remove the catalyst particles prior to analysis. To quantify the intermediates formed during the reaction, the samples were analyzed by high-performance liquid chromatography (HPLC). The HPLC consisted of an isocratic pump (Waters 501), a Rheodyne injector, C-18 column, UV detector (Waters 2487), and a data acquisition system. The eluent system consisted of 90 vol. % water, and 10 vol. % methanol pumped at 0.5 mL/min. Though in this eluent system the substituted phenols elute only after 30–45 min, it ensures that the peaks of intermediates are well separated. Samples were injected in a Rheodyne valve with a sample loop of 50  $\mu$ L, and the UV absorbances at 280 nm for phenol, 4-chlorophenol, 2, 4-dinitrophenol, 4-chloro-2-nitrophenol and 2-chloro-4-nitrophenol, and 4-methylphenol and at 320 nm for 4-nitrophenol and 2-nitrophenol were monitored. The chromatographic areas were converted to concentration values using calibration curves based on pure compounds.

## Results and Discussion

**Crystal Structure of Ba<sub>2</sub>Bi<sub>24</sub>Mo<sub>10</sub>O<sub>68</sub>.** Ba<sub>2</sub>Bi<sub>24</sub>Mo<sub>10</sub>O<sub>68</sub> crystallizes in the monoclinic *P*2/*c* space group (No. 13) with *a* = 11.688(4) Å, *b* = 5.813(1) Å, *c* = 24.715(7) Å,  $\beta$  = 101.838(4)°, *V* = 1643.8(8) Å<sup>3</sup>, and *Z* = 8. Initially, the coordinates of Bi, Ba, and Mo were obtained by the direct methods. The oxygen atoms were located by subsequent difference Fourier syntheses. Atoms Bi(1)–Bi(6), Mo(1), and Mo(3) occupy the general positions. Ba(1) occupies the 2*a* site while O(1) and O(2) occupy the 2*f* sites. The remaining oxygen atoms occupy the general positions. The structure is related to the fluorite type with *b*  $\approx$  *a<sub>F</sub>* and *c* = 5*a<sub>F</sub>* where *a<sub>F</sub>* represents the fluorite unit cell parameter. The crystal structure along the

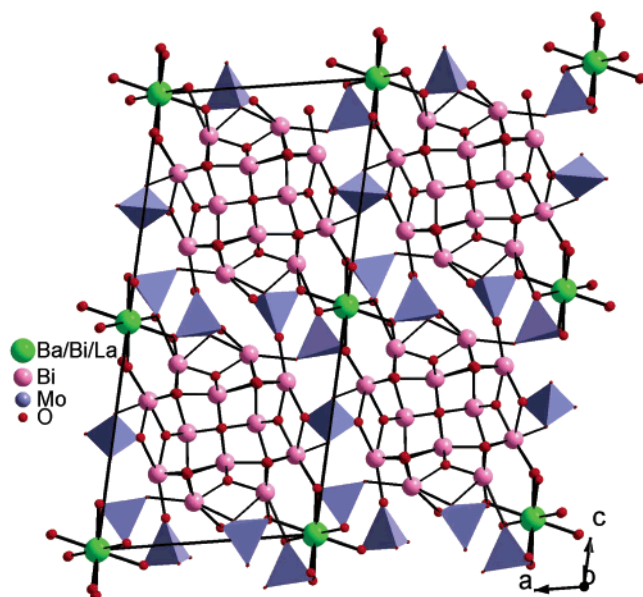


Figure 1. Crystal structure of  $\text{Ba}_2\text{Bi}_{24}\text{Mo}_{10}\text{O}_{68}$  viewed along the  $b$  axis.

TABLE 2: Selected Bond Distances (Å) of  $\text{Ba}_2\text{Bi}_{24}\text{Mo}_{10}\text{O}_{68}$

Bi(1)	—O(1)	2.663(13)	Bi(2)	—O(1)	2.116(9)
	—O(2)	2.164(9)		—O(2)	2.587(13)
	—O(3)	2.918(15)		—O(3)	2.372(14)
	—O(4)	2.375(15)		—O(5)	2.351(15)
	—O(5)	2.987(15)		—O(6)	2.876(15)
	—O(6)	2.420(16)		—O(7)	2.253(15)
	—O(8)	2.224(17)			
	—O(9)	2.98(2)			
Bi(3)	—O(4)	2.121(16)	Bi(4)	—O(3)	2.193(14)
	—O(5)	2.185(16)		—O(6)	2.135(14)
	—O(7)	2.253(15)		—O(7)	2.159(16)
	—O(10)	2.67(2)		—O(10)	2.670(19)
	—O(14)	2.78(3)		—O(12)	2.54(2)
	—O(16)	2.95(2)		—O(17)	2.64(3)
	—O(8)	2.87(3)			
			Bi(6)	—O(4)	2.162(15)
Bi(5)	—O(3)	2.091(14)		—O(5)	2.112(15)
	—O(6)	2.155(14)		—O(8)	2.135(16)
	—O(8)	2.166(18)		—O(9)	2.79(3)
	—O(9)	2.86(3)		—O(11)	2.87(2)
	—O(13)	2.44(3)		—O(15)	2.75(3)
				—O(18)	2.67(4)
Ba(1)	—O(11) × 2	2.54(3)	Mo(1)	—O(10)	1.74(2)
	—O(14) × 2	2.62(3)		—O(13)	1.76(3)
	—O(15) × 2	2.96(3)		—O(14)	1.77(3)
	—O(16) × 2	2.99(4)		—O(17)	1.69(3)
Mo(3)	—O(11)	1.72(2)			
	—O(12)	1.76(3)			
	—O(15)	1.70(2)	Mo(2)	—O(9) × 2	1.73(2)
	—O(16)	1.75(2)		—O(18) × 2	1.61(4)

$b$  axis (Figure 1) consists of columns of  $[\text{Bi}_{12}\text{O}_{14}]$  units similar to the parent compound,  $\text{Bi}_{26}\text{Mo}_{10}\text{O}_{69}$ .<sup>8</sup> Each  $[\text{Bi}_{12}\text{O}_{14}]$  unit resembles a “rose” built of Bi(1)—Bi(6) atoms yielding a  $[\text{Bi}_{12}\text{O}_{14}]_{\infty}$  network extending along the 2-fold axis (Figure 1) and is surrounded by the noncolumnar Ba atoms and  $\text{MoO}_4$  tetrahedra. Each column is surrounded by eight  $\text{MoO}_4$  tetrahedra.

All bismuth atoms exhibit an irregular one-sided coordination (2.164–2.99 Å) owing to the presence of the  $6s^2$  lone pair (Table 2). The coordination numbers of atoms Bi(2)—Bi(8) vary from five to eight while Bi(1) forms Bi(1) $\text{O}_9$  polyhedra. However,  $\text{Bi}_{26}\text{Mo}_{10}\text{O}_{69}$  shows a maximum coordination number of eight for Bi atoms. It is noteworthy that the noncolumnar Ba atom also exhibits eight coordination with bond distances (2.54–2.99 Å) similar to the Bi(7) atom in  $\text{Bi}_{26}\text{Mo}_{10}\text{O}_{69}$ . As in the parent

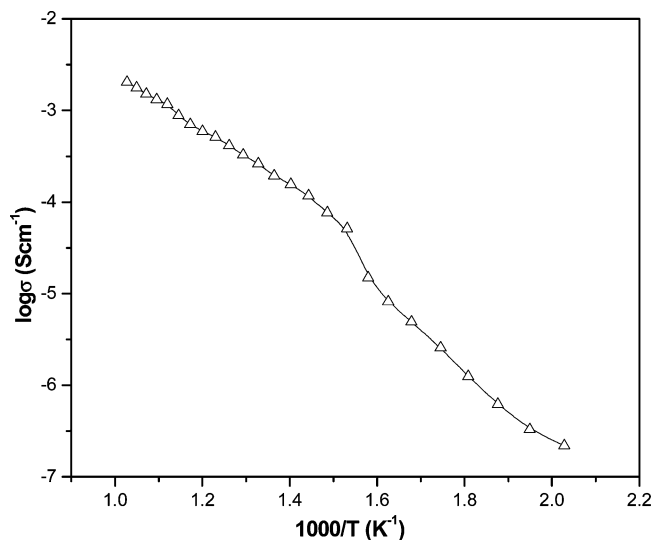


Figure 2. Conductivity Arrhenius plot of  $\text{La}_2\text{Bi}_{24}\text{Mo}_{10}\text{O}_{69}$ .

structure, the  $\text{MoO}_4$  tetrahedra are isolated in  $\text{Ba}_2\text{Bi}_{24}\text{Mo}_{10}\text{O}_{68}$  and the Mo—O distances are in the range (1.61–1.76 Å).

$\text{La}_2\text{Bi}_{24}\text{Mo}_{10}\text{O}_{69}$  also crystallizes in the monoclinic  $P2_1/c$  space group (No. 13), with  $a = 11.7586(28)$  Å,  $b = 5.7779(14)$  Å,  $c = 24.6489(60)$  Å,  $\beta = 102.060(4)^\circ$ ,  $V = 1640.08(4)$  Å<sup>3</sup>, and  $Z = 8$ . Owing to the poor quality of the crystal, accurate coordinates of oxygen atoms could not be obtained. Repeated attempts at crystallization did not yield better quality crystals.

**Differential Scanning Calorimetry (DSC).**  $\text{Ba}_2\text{Bi}_{24}\text{Mo}_{10}\text{O}_{68}$  does not show any phase transition.  $\text{La}_2\text{Bi}_{24}\text{Mo}_{10}\text{O}_{69}$  undergoes an endothermic phase transition (See Figure S2 in Supporting Information) around 310 °C with a thermal hysteresis characteristic of a first-order phase transition similar to that of  $\text{Bi}_{26}\text{Mo}_{10}\text{O}_{69}$ .<sup>8</sup> The reversible phase transition was reported as a monoclinic—triclinic transition. Heat capacities,  $C_p$ , for both the phases were calculated, and the enthalpy of transition was estimated by integration with respect to  $T$  and  $\ln T$ , respectively. The enthalpy of phase transition of  $\text{Bi}_{26}\text{Mo}_{10}\text{O}_{69}$  ( $\Delta H = 548.59$  cal/mol) was found to be larger than that of  $\text{La}_2\text{Bi}_{24}\text{Mo}_{10}\text{O}_{69}$  (172.4 cal/mol). Thermogravimetric analysis showed no loss in weight suggesting that the room-temperature structure undergoes a structural variation at high temperature without change in composition.

**ac Impedance.** The variation of conductivity with respect to temperature for  $\text{La}_2\text{Bi}_{24}\text{Mo}_{10}\text{O}_{69}$  is shown in Figure 2. The order of conductivity is the same as that for  $\text{Bi}_{26}\text{Mo}_{10}\text{O}_{69}$ .<sup>8</sup> However,  $\text{Ba}_2\text{Bi}_{24}\text{Mo}_{10}\text{O}_{68}$  shows conductivity of an order less in magnitude than that of the trivalent-substituted compounds.<sup>11</sup> The Arrhenius plot of  $\text{La}_2\text{Bi}_{24}\text{Mo}_{10}\text{O}_{69}$  shows a change in slope (Figure 2) around 310 °C indicative of a phase transition further confirmed by DSC studies. The high conductivity with increase in temperature is attributed to the exchange of oxygen between  $\text{MoO}_4$  tetrahedra via a cooperative motion.

**UV–vis Spectra.** The UV–vis spectra of  $\text{Bi}_{26}\text{Mo}_{10}\text{O}_{69}$ ,  $\text{La}_2\text{Bi}_{24}\text{Mo}_{10}\text{O}_{69}$ , and  $\text{Ba}_2\text{Bi}_{24}\text{Mo}_{10}\text{O}_{68}$  are shown in Figure 3. To obtain precise values of band gap from the absorption edges, the point of inflection determined from the minimum in the first derivative of the absorption spectrum was used. Substitution of ions at the noncolumnar Bi site results in a decrease in the band gap with values of 3.22, 2.9, and 2.74 eV for  $\text{Bi}_{26}\text{Mo}_{10}\text{O}_{69}$ ,  $\text{La}_2\text{Bi}_{24}\text{Mo}_{10}\text{O}_{69}$ , and  $\text{Ba}_2\text{Bi}_{24}\text{Mo}_{10}\text{O}_{68}$ , respectively.

**Photocatalysis. Degradation Reactions.** The photocatalytic activity of  $\text{Ba}_2\text{Bi}_{24}\text{Mo}_{10}\text{O}_{68}$  was checked by performing the degradation of phenol, 4-nitrophenol, 4-chlorophenol, and



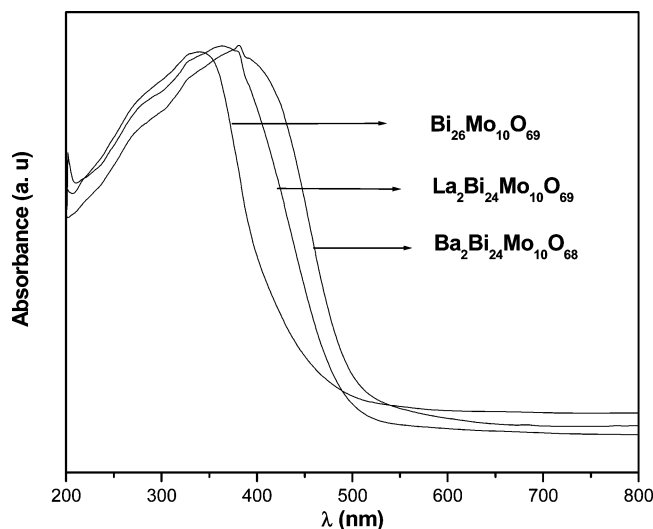


**Figure 3.** UV-vis spectra of  $\text{Bi}_{26}\text{Mo}_{10}\text{O}_{69}$ ,  $\text{La}_2\text{Bi}_{24}\text{Mo}_{10}\text{O}_{69}$ , and  $\text{Ba}_2\text{Bi}_{24}\text{Mo}_{10}\text{O}_{68}$ .

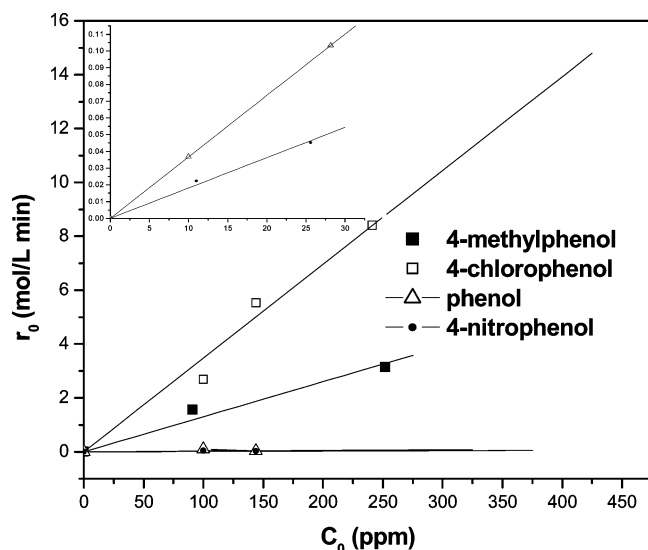


**Figure 4.** Variation of initial rates with concentration for phenol and substituted phenols in the presence of  $\text{Ba}_2\text{Bi}_{24}\text{Mo}_{10}\text{O}_{69}$ . The inset shows the enlarged plots for phenol and 4-nitrophenol.

4-methylphenol under UV radiation in the presence of  $\text{Ba}_2\text{Bi}_{24}\text{Mo}_{10}\text{O}_{68}$ . The concentration profiles of the degradation reactions indicate that they are all first order. Owing to negligible surface area in compounds synthesized by the ceramic method, the equilibrium adsorption is negligible. Hence the first-order rate expression,  $r_0 = k_0 C_0$ , was used where  $k_0$  denotes the rate coefficient,  $C_0$  represents the initial concentration, and  $r_0$  denotes the initial photocatalytic degradation rate.

Figure 4 shows the variation of the initial photocatalytic degradation rate,  $r_0$ , with initial concentration,  $C_0$ , for degradation of phenol and substituted phenols in the presence of  $\text{Ba}_2\text{Bi}_{24}\text{Mo}_{10}\text{O}_{68}$ . The rate constant for the degradation of phenol in the presence of  $\text{Ba}_2\text{Bi}_{24}\text{Mo}_{10}\text{O}_{68}$  was  $0.0037 \text{ min}^{-1}$ . The photocatalytic degradation rate of 4-chlorophenol was  $\sim 9.4$  times that of phenol and thrice that of 4-methylphenol (Table 3, Figure 4). The enhanced degradation of 4-chlorophenol and 4-methylphenol compared to that of phenol is consistent with earlier studies<sup>20</sup> with commercial titania (Degussa P-25) and combustion synthesized titania catalysts. This enhancement is attributed to the deactivating nature of the substituents in the aromatic ring<sup>21</sup> since the hydroxyl radical attacks the position of substitution (chloro or methyl) and not the ring.

**TABLE 3: First-Order Initial Photocatalytic Rate Constants of  $\text{Ba}_2\text{Bi}_{24}\text{Mo}_{10}\text{O}_{69}$ ,  $\text{La}_2\text{Bi}_{24}\text{Mo}_{10}\text{O}_{69}$ , and  $\text{Bi}_{26}\text{Mo}_{10}\text{O}_{69}$**

catalyst	pollutant	$k \text{ (min}^{-1}\text{)}$	$k_{\text{pollutant}}/k_{\text{phenol}}$
$\text{Ba}_2\text{Bi}_{24}\text{Mo}_{10}\text{O}_{69}$	phenol	0.0037	1
	2-nitrophenol	0.0028	0.75
	4-chlorophenol	0.0348	9.41
	4-nitrophenol	0.0018	0.49
	4-methylphenol	0.013	3.51
	2,4-dinitrophenol	0.0026	0.70
	4-chloro-2-nitrophenol	0.0029	0.78
$\text{La}_2\text{Bi}_{24}\text{Mo}_{10}\text{O}_{69}$	4-nitro-2-chlorophenol	0.0075	2.03
	phenol	0.0121	3.27
$\text{Bi}_{26}\text{Mo}_{10}\text{O}_{69}$	2,4-dinitrophenol	0.0067	1.81
	phenol	0.0063	1.7
	2,4-dinitrophenol	0.0033	0.89

The degradation rate of 4-nitrophenol in the presence of  $\text{Ba}_2\text{Bi}_{24}\text{Mo}_{10}\text{O}_{69}$  (inset of Figure 4) was the least of all the substituted phenols and is nearly half of that of phenol. However, in the presence of Degussa P25 and combustion synthesized titania, the degradation rate of 4-nitrophenol is higher than that of phenol.<sup>22</sup> As the trend for degradation of 4-nitrophenol was different in the presence of  $\text{Ba}_2\text{Bi}_{24}\text{Mo}_{10}\text{O}_{69}$ , the position effect of the nitro substituent was investigated by degrading 2-nitrophenol. The degradation rate of 2-nitrophenol was found to be higher than that of 4-nitrophenol (Figure 5a, Table 3), which is also in contrast to the results<sup>23</sup> obtained in the presence of Degussa P25. This indicates that the catalyst is nitro specific.

To estimate the influence of the position of the nitro group in the presence of other substituents such as chlorine in the aromatic ring, the degradation reactions of 4-chloro-2-nitrophenol, 4-nitro-2-chlorophenol, and 2,4-dinitrophenol were performed. The degradation rate of 4-nitro-2-chlorophenol was found to be faster than that of 4-chloro-2-nitrophenol (Figure 5b) indicating that the chloro substituent in the aromatic ring influences degradation more than the nitro group. The rates of degradation of 2,4-dinitrophenol and 4-chloro-2-nitrophenol were found to be nearly the same as that of 2-nitrophenol (Table 3). This indicates that the influence of nitro substituent at the ortho position in the aromatic ring is greater in the presence of other substituents such as chlorine. However, the influence of nitro substituent at the para position appears subdued in the presence of other substituents as evident from the higher value of rate constant observed for 4-nitro-2-chlorophenol than for 4-nitrophenol. The overall order of degradation rates in the presence of  $\text{Ba}_2\text{Bi}_{24}\text{Mo}_{10}\text{O}_{68}$  can be elucidated as 4-chlorophenol > 4-methylphenol > phenol > 4-nitro-2-chlorophenol > 4-chloro-2-nitrophenol  $\approx$  2,4-dinitrophenol  $\approx$  2-nitrophenol > 4-nitrophenol.

The next objective of this work was to study the effect of substitution of  $\text{La}^{3+}$  at the noncolumnar site on photocatalytic activity. The degradation reaction of phenol was carried out in the presence of  $\text{La}_2\text{Bi}_{24}\text{Mo}_{10}\text{O}_{69}$  and  $\text{Bi}_{26}\text{Mo}_{10}\text{O}_{69}$ . To verify if these compounds are nitro specific, the degradation of 2,4-dinitrophenol (Figure 6a) was also performed with these catalysts. The degradation rates of phenol and 2,4-dinitrophenol in the presence of  $\text{La}_2\text{Bi}_{24}\text{Mo}_{10}\text{O}_{69}$  was found to be higher than that in the presence of either  $\text{Ba}_2\text{Bi}_{24}\text{Mo}_{10}\text{O}_{68}$  or  $\text{Bi}_{26}\text{Mo}_{10}\text{O}_{69}$  leading to the order of activity of degradation as  $\text{La}_2\text{Bi}_{24}\text{Mo}_{10}\text{O}_{69} > \text{Bi}_{26}\text{Mo}_{10}\text{O}_{69} > \text{Ba}_2\text{Bi}_{24}\text{Mo}_{10}\text{O}_{68}$  (Table 3). Though  $\text{Ba}_2\text{Bi}_{24}\text{Mo}_{10}\text{O}_{68}$  has a lower value of band gap, it shows the least activity. This implies differences in their electronic structures. In bismuth(III)-based semiconductors, the Bi 6s and O 2p orbitals form a hybridized valence band. In terms of this description, we assume that the valence band of  $\text{Bi}_{26}\text{Mo}_{10}\text{O}_{69}$  is composed of hybridized Bi 6s and O 2p orbitals, whereas

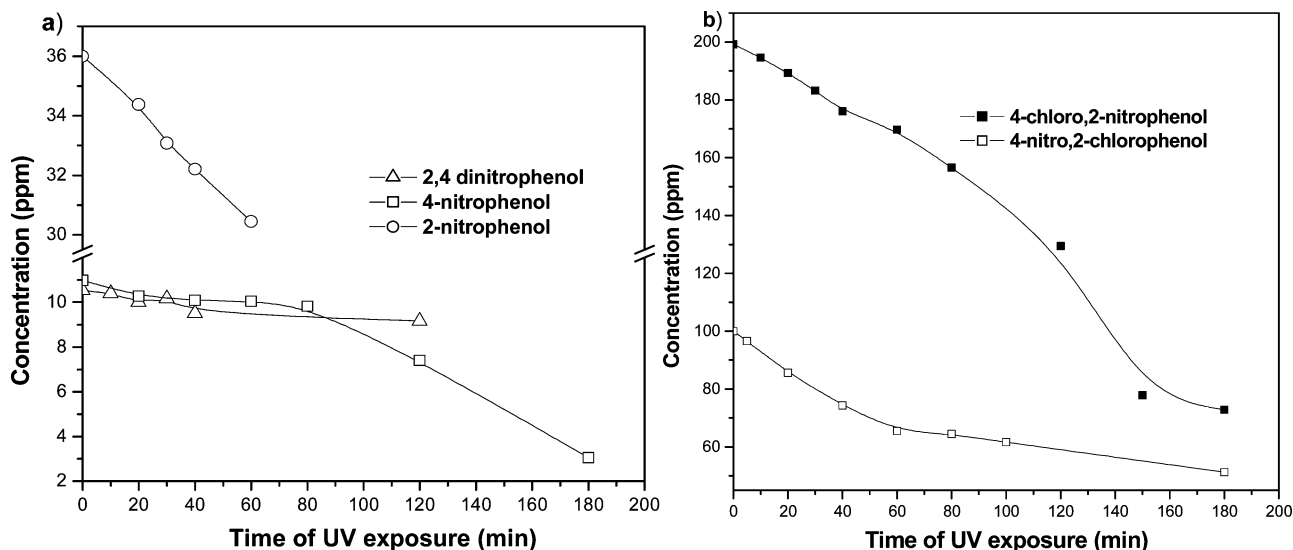
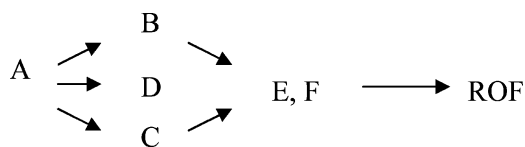


Figure 5. Degradation profiles of (a) chloronitrophenols and (b) nitrophenols in the presence of  $\text{Ba}_2\text{Bi}_{24}\text{Mo}_{10}\text{O}_{68}$ .

the conduction band is composed of hybridized Bi 6p and Mo 4d orbitals, and these bands meet the potential requirements of a photocatalytic oxidation. Since Ba and La atoms occupy the noncolumnar Bi site, mixing of Bi 6s and La valence orbitals should occur in the valence band of  $\text{La}_2\text{Bi}_{24}\text{Mo}_{10}\text{O}_{69}$ . Similarly, the valence band of  $\text{Ba}_2\text{Bi}_{24}\text{Mo}_{10}\text{O}_{68}$  should consist of hybridized Bi 6s and Ba 5p orbitals. The better photocatalytic activity may imply larger overlap of the hybridized orbitals of valence and conduction bands in  $\text{La}_2\text{Bi}_{24}\text{Mo}_{10}\text{O}_{69}$  than in  $\text{Bi}_{26}\text{Mo}_{10}\text{O}_{69}$  and  $\text{Ba}_2\text{Bi}_{24}\text{Mo}_{10}\text{O}_{68}$ .

**Intermediates Analysis.** To determine the reaction kinetics of photocatalytic degradation, a model was developed for determining the rates of formation and consumption of intermediates. The concentration of all the intermediates increases initially and then decreases. The maximum in the concentration of the intermediates is observed due to the competition between the primary hydroxylation and the secondary hydroxylation step. The degradation pathway for the pollutants thus can be described as follows



where A is the degraded pollutant, B, C, and D are the intermediates formed due to primary hydroxylation, E and F are formed due to secondary hydroxylation, and ROF denotes ring-opened fragments. Since the reactions follow first-order kinetics and for a series of reactions with  $k_f$  and  $k_c$  denoting the rate coefficient for formation and consumption of intermediates, respectively, the concentration of the intermediate,  $C_{\text{int}}$ , is

$$\frac{C_{\text{int}}}{C_{\text{A0}}} = \frac{k_f}{k_c - k_f} (\exp(-k_f t) - \exp(-k_c t))$$

where  $C_{\text{A0}}$  is the initial concentration of the pollutant. The maximum concentration of the intermediate,  $C_{\text{int,max}}$ , can be obtained from the above equation and is

$$\frac{C_{\text{int,max}}}{C_{\text{A0}}} = \left( \frac{k_f}{k_c} \right)^{1/(1-k_f/k_c)}$$

and

$$t_{\text{max}} = \frac{\ln\left(\frac{k_f}{k_c}\right)}{k_c\left(\frac{k_f}{k_c} - 1\right)}$$

The concentration of the intermediates from the experimental data was fit using the above equations to determine the kinetic rate coefficients.

HPLC analysis of the degradation reactions revealed the sequential formation and degradation of intermediates in the presence of  $\text{La}_2\text{Bi}_{24}\text{Mo}_{10}\text{O}_{69}$ ,  $\text{Bi}_{26}\text{Mo}_{10}\text{O}_{69}$ , and  $\text{Ba}_2\text{Bi}_{24}\text{Mo}_{10}\text{O}_{68}$ . Three common intermediates were detected for phenol in the presence of all the three catalysts (Figure 6b). The intermediates were detected as catechol, hydroquinone, and organic acids (primarily a mixture of oxalic acid and maleic acid), which form as a result of ring opening during degradation. These intermediates are the same as that obtained for the degradation of phenol by titania.<sup>23</sup> The concentration of organic acids was not quantified, but the mineralization of phenol to organic acids,  $\text{CO}_2$ , and water can be obtained by mass balance. For example, the degradation of 28 ppm of phenol after 3 h by  $\text{Ba}_2\text{Bi}_{24}\text{Mo}_{10}\text{O}_{68}$  resulted in the reduction of phenol concentration to 10.6 ppm and the concentrations of intermediates hydroquinone and catechol were 6.3 and 4.4 ppm. The mass balance indicates that the total mineralization to organic acids and ROF is 6.7 ppm.

In the case of the degradation of 4-chlorophenol, two more intermediates were detected along with hydroquinone and catechol, which were assigned as hydroxy hydroquinone and 4-chlorocatechol. Figure 7a shows the concentration profiles and the model fit of hydroquinone, 4-chlorocatechol, and phenol (Inset of Figure 7a) formed during the degradation of 4-chlorophenol. The amounts of hydroquinone formed during the degradation of phenol and 4-chlorophenol were higher than that of catechol formed. The degradation pathway for 4-chlorophenol occurs via 4-chlorocatechol, which is similar to that in the presence of Degussa P-25.<sup>25</sup>

The degradation of 4-methylphenol resulted in three intermediates, hydroquinone and catechol (in small amounts) and phenol (inset of Figure 7b). Interestingly, there were no detectable intermediates in the case of 4-nitrophenol, 2-nitro-

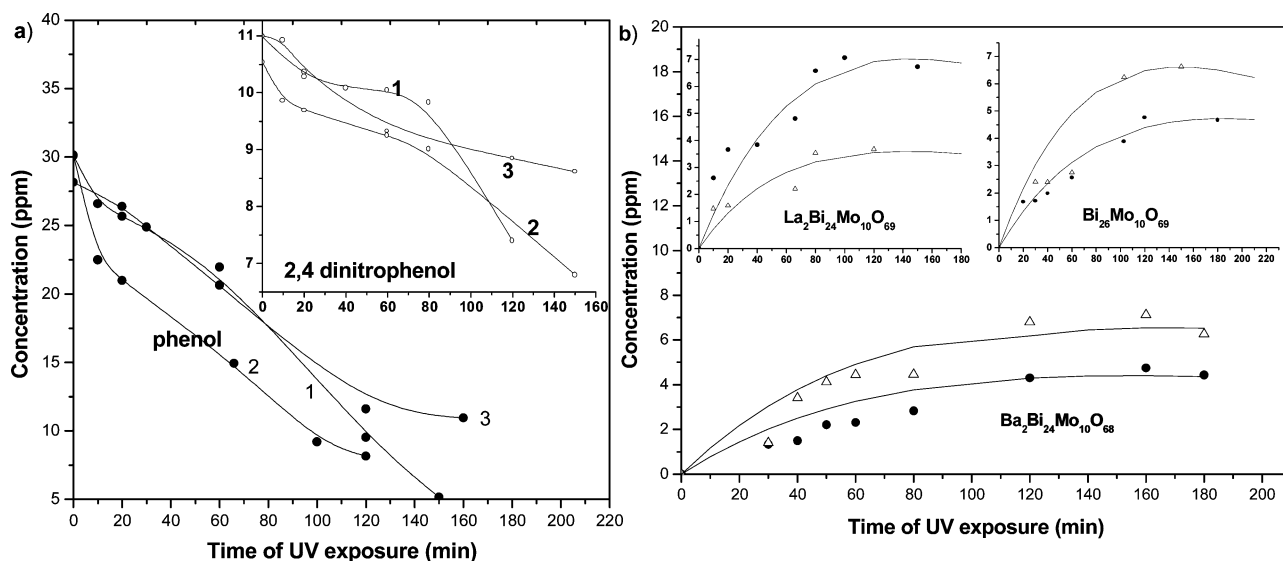


**Figure 6.** Degradation profiles of (a) phenol and 2,4-dinitrophenol in the presence of  $\text{Ba}_2\text{Bi}_{24}\text{Mo}_{10}\text{O}_{68}$  (1),  $\text{La}_2\text{Bi}_{24}\text{Mo}_{10}\text{O}_{69}$  (2), and  $\text{Bi}_{26}\text{Mo}_{10}\text{O}_{69}$  (3). (b) Concentration profiles of intermediates hydroquinone ( $\Delta$ ) and catechol ( $\bullet$ ) for degradation of phenol with the lines indicating model fit.

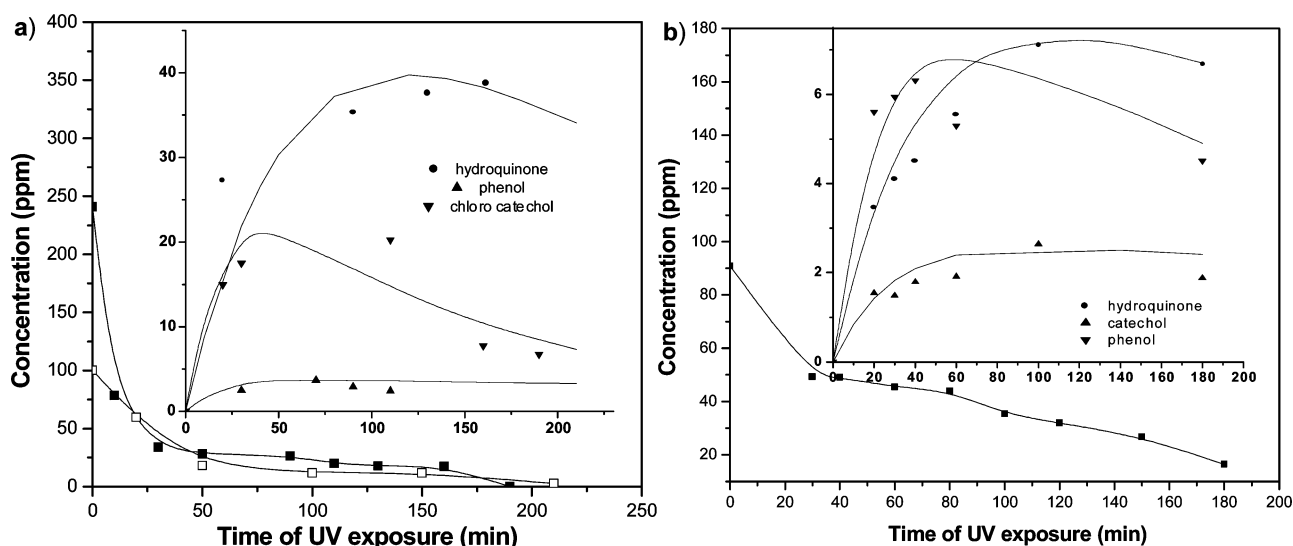


**Figure 7.** Degradation profiles of (a) 4-chlorophenol and (b) 4-methylphenol in the presence of  $\text{Ba}_2\text{Bi}_{24}\text{Mo}_{10}\text{O}_{68}$ . The insets show concentration profiles of intermediates with the lines indicating model fit.

**TABLE 4: The Formation and Consumption Rate Constants of Various Intermediates for  $\text{Ba}_2\text{Bi}_{24}\text{Mo}_{10}\text{O}_{68}$ ,  $\text{La}_2\text{Bi}_{24}\text{Mo}_{10}\text{O}_{69}$ , and  $\text{Bi}_{26}\text{Mo}_{10}\text{O}_{69}$**

catalyst	pollutant	intermediates	$k_f$ ( $\text{min}^{-1}$ )	$k_c$ ( $\text{min}^{-1}$ )	$k_c/k_f$
$\text{Ba}_2\text{Bi}_{24}\text{Mo}_{10}\text{O}_{68}$	phenol	hydroquinone	0.0045	0.01	2.2
		catechol	0.003	0.012	4
	4-chlorophenol	hydroquinone	0.004	0.015	3.8
		phenol	0.001	0.06	60
	4-methylphenol	4-chlorocatechol	0.007	0.06	8.6
		hydroquinone	0.002	0.023	11.5
$\text{La}_2\text{Bi}_{24}\text{Mo}_{10}\text{O}_{69}$	phenol	catechol	0.001	0.035	35
		phenol	0.004	0.04	10
		hydroquinone	0.003	0.015	5
$\text{Bi}_{26}\text{Mo}_{10}\text{O}_{69}$	phenol	catechol	0.005	0.010	2
		hydroquinone	0.004	0.010	2.5
		catechol	0.003	0.010	3.3

phenol, 2,4-dinitrophenol, and 4-nitro-2-chlorophenol while hydroquinone was the only intermediate detected for 4-chloro-2-nitrophenol.

The insets of Figures 6 and 7 show that the model prediction closely represents the formation of intermediates. In general, the consumption rate of intermediates appears to be faster than its formation (Table 4). The ratios of consumption to formation

rate constants for catechol formed during the degradation of phenol in the presence of  $\text{Ba}_2\text{Bi}_{24}\text{Mo}_{10}\text{O}_{68}$ ,  $\text{La}_2\text{Bi}_{24}\text{Mo}_{10}\text{O}_{69}$ , and  $\text{Bi}_{26}\text{Mo}_{10}\text{O}_{69}$  are 4, 2, and 3.3, respectively.

The consumption rate constant of catechol intermediate for 4-methylphenol in the presence of  $\text{Ba}_2\text{Bi}_{24}\text{Mo}_{10}\text{O}_{68}$  is nearly 35 times its formation rate than that of phenol ( $\sim 10$  times) indicating that catechol remains in smaller amounts in the system

for a longer time than the other intermediates (inset of Figure 7b). A similar trend was exhibited by the phenol intermediate ( $k_c/k_f = 60$ ) during the degradation of 4-chlorophenol. The high ratio of the intermediate consumption rate coefficient to the intermediate formation rate clearly demonstrates the destabilization of phenol due to substitution. However, since no intermediates were detected during the degradation of 4-nitrophenol, the pathway of degradation seems to be different with this catalyst.

It can be inferred that there was no formation of primary hydroxylated products such as hydroxynitrophenol, hydroxychlorophenol, and hydroxymethylphenol. The hydroxyl radical preferentially attacks the substituted methyl group or chlorine and not the ring to favor degradation leading to an increased degradation of chloro- and methylphenols compared to that of phenol. The preference of attack on the methyl group is lesser as compared to the attack on chloro substitution, consistent with previous studies with commercial titania. However, the ability of this catalyst to degrade nitrophenols is much less than that of commercial titania. The reason for the observed selectivity is not apparent. This selectivity in hydroxylation may be useful in controlling the formation of specific desired products.

### Summary

$\text{Ba}_2\text{Bi}_{24}\text{Mo}_{10}\text{O}_{68}$ ,  $\text{La}_2\text{Bi}_{24}\text{Mo}_{10}\text{O}_{69}$ , and  $\text{Bi}_{26}\text{Mo}_{10}\text{O}_{69}$  were synthesized by the ceramic route. The crystal structures of  $\text{Ba}_2\text{Bi}_{24}\text{Mo}_{10}\text{O}_{68}$  and  $\text{La}_2\text{Bi}_{24}\text{Mo}_{10}\text{O}_{69}$  are isostructural to that of  $\text{Bi}_{26}\text{Mo}_{10}\text{O}_{69}$  with differences in the coordination of the atom at the noncolumnar atom site. The compounds were used to degrade phenol and various substituted phenols. All the three compounds show nitro specificity and also favor degradation when nitro substituent is present at the ortho position in the aromatic ring. Despite high band gaps,  $\text{La}_2\text{Bi}_{24}\text{Mo}_{10}\text{O}_{69}$  and  $\text{Bi}_{26}\text{Mo}_{10}\text{O}_{69}$  show higher activity than  $\text{Ba}_2\text{Bi}_{24}\text{Mo}_{10}\text{O}_{68}$ . This behavior may be attributed to larger overlap of the hybridized orbitals of valence and conduction bands in  $\text{La}_2\text{Bi}_{24}\text{Mo}_{10}\text{O}_{69}$  than in  $\text{Bi}_{26}\text{Mo}_{10}\text{O}_{69}$  and  $\text{Ba}_2\text{Bi}_{24}\text{Mo}_{10}\text{O}_{68}$ .

**Acknowledgment.** We thank the Department of Science and Technology, India for data collection on the CCD facility under the IRPHA-DST program and Dr. A. K. Tyagi, BARC, Mumbai for high-temperature X-ray powder diffraction data. B. Muktha thanks CSIR for a senior research fellowship.

**Supporting Information Available:** CIF crystal data for  $\text{Ba}_2\text{Bi}_{24}\text{Mo}_{10}\text{O}_{68}$  and X-ray powder profile and DSC plot of  $\text{La}_2\text{Bi}_{24}\text{Mo}_{10}\text{O}_{69}$ . This material is available free of charge via the Internet at <http://pubs.acs.org>.

### References and Notes

- (1) Boivin, J. C.; Mairesse, G. *Chem. Mater.* **1998**, *10*, 2870.
- (2) Kendall, K. R.; Navas, C.; Thomas, J. K.; zur Loye, H.-C. *Chem. Mater.* **1996**, *8*, 642.
- (3) Subbarao, E. L. *J. Phys. Chem. Solids* **1962**, *23*, 665.
- (4) Graselli, R. K. *J. Chem. Educ.* **1986**, *63*, 216.
- (5) Le, M. T.; Van Craenenbroeck, J.; Van Driessche, I.; Hoste, S. *Appl. Catal. A* **2003**, *249*, 355.
- (6) Buttrey, D. J.; Jefferson, D. A.; Thomas, J. M. *Philos. Mag. A* **1986**, *53*, 897.
- (7) Shuk, P.; Wiemhofer, H.-D.; Guth, U.; Gopel, W.; Greenblatt, M. *Solid State Ionics* **1993**, *89*, 179.
- (8) Vannier, R. N.; Mairesse, G.; Abraham, F.; Nowogrocki, G. *J. Solid State Chem.* **1996**, *122*, 394.
- (9) Enjalbert, R.; Hasselmann, G. J. Galy, *Acta Crystallogr., C* **1997**, *53*, 269.
- (10) Castro, A.; Enjalbert, R.; Baules, P.; Galy, J. *J. Solid State Chem.* **1998**, *185*, 11.
- (11) Vannier, R. N.; Danze, S.; Nowogrocki, G.; Huve, M.; Mairesse, G. *J. Solid State Ionics* **2000**, *136–137*, 51.
- (12) Muktha, B.; Guru Row: T. N. *Struct. Chem.*, in press.
- (13) Grins, J.; Esmailzadeh, S.; Hull, S. *J. Solid State Chem.* **2002**, *163*, 144.
- (14) Galy, J.; Enjalbert, R.; Rozier, P.; Millet, P. *Solid State Sci.* **2003**, *5*, 165.
- (15) Bruker. SMART and SAINT. Bruker AXS Inc., Madison, WI, 1998.
- (16) Sheldrick, G. M. SHELXL97. Program for crystal structure refinement; University of Gottingen, Germany, 1997.
- (17) Petricek, V.; Dusek, M. Jana 2000. Structure Determination Software Programs; Institute of Physics, Praha, Czech Republic, 2000.
- (18) Sivalingam, G.; Nagaveni, K.; Hegde, M. S.; Madras, G. *Appl. Catal., B* **2003**, *45*, 23.
- (19) Buttrey, D. J.; Vogt, T.; Wildgruber, U.; Robinson, W. R. *J. Solid State Chem.* **1994**, *111*, 118.
- (20) Sivalingam, G.; Priya, H. M.; Madras, G. *Appl. Catal., B* **2004**, *51*, 67.
- (21) Wang, K. H.; Hsieh, Y. H.; Chen, L. J. *J. Hazard. Mater.* **1998**, *59*, 251.
- (22) Nagaveni, K.; Sivalingam, G.; Hegde, M. S.; Madras, G. *Environ. Sci. Technol.* **2004**, *38*, 1600.
- (23) Priya, M. H.; Madras, G. *J. Photochem. Photobiol., A* **2006**, *178*, 1.
- (24) Hoffmann, M. R.; Martin, S. T.; Choi, W.; Bahnemann, D. W. *Chem. Rev.* **1995**, *95*, 69.
- (25) Theurich, J.; Lindner, M.; Bahnemann, D. W. *Langmuir* **1996**, *12*, 6368.